Supporting information

Bimetallic ZnSe-SnSe$_2$ heterostructure functionalized separator for high-rate Li-S batteries

1. Materials and Methods

1.1 Materials

Urea (AR, Sinopharm Chemical Reagent Co., Ltd)，zinc sulfate heptahydrate (AR, Sinopharm Chemical Reagent Co., Ltd)，sodium stannate trihydrate (AR, Sinopharm Chemical Reagent Co, Ltd), polyvinylidene fluoride (Aldrich, Sigma Aldrich, Co.)，glucose (AR, Sinopharm Chemical Reagent Co., Ltd), Selenium (AR，Aladdin Bio-Chem Technology Co., Ltd)，sulfur powder (Aladdin Bio-Chem Technology Co., Ltd)，N-methyl-2-pyrrolidone solution (Aldrich, Sigma Aldrich, Co.), lithium sulfide (Li$_2$S, Alfa Aesar Chemical Co., Ltd), Super-P (HF-Kejing Co., Ltd).

1.2 Preparation Methods

1.2.1 Synthesis of OCN, ZnSn(OH)$_6$@OCN and ZnSe-SnSe$_2$@OCN

For OCN Material, OCN was prepared according to our previously reported method[1, 2]. A suitable amount of urea and glucose solid mixture with a weight ratio of 10:1 was added to a crucible with a tightly fastened cover. The covered crucible was heated in a muffle oven with a program-controlled temperature system. The chamber of the muffle oven is under ambient pressure and is not protected by any inert atmosphere. The temperature was first raised to 550 °C for 1 h, then down to 200 °C for 0.5 h, and finally, the temperature was brought to 900 °C for another 1 h. Then, the temperature was allowed to naturally decline to 296 K (23 °C).

For ZnSn(OH)$_6$@OCN material, a mixture of 372 mg sodium stannate trihydrate (Na$_2$SnO$_3$·3H$_2$O) and 400 mg zinc sulfate heptahydrate (ZnSO$_4$·7H$_2$O) was dissolved

in 250 mL of deionized water. After complete dissolution, 400 mg of OCN was added and the solution was stirred overnight. Subsequently, the mixture was transferred to a drying oven at 80 °C and dried until the solvent completely evaporated, yielding a powder denoted as $ZnSn(OH)_6@OCN$.

For $ZnSe-SnSe_2@OCN$, the mixture of 200 mg $ZnSn(OH)_6@OCN$ and 400 mg selenium powder was thoroughly ground. The resulting mixture was then placed in a tubular furnace under a hydrogen-argon atmosphere, and the temperature was raised to 300 °C and maintained for 3 h. Subsequently, the temperature was further increased to 500 °C and held for 2 h for calcination. After naturally cooling to room temperature, a black substance designated as $ZnSe-SnSe_2@OCN$ was obtained.

1.2.2 Preparation of Super P /S cathodes and functionalized separators

The Super P and sulfur (in a 3:7 mass ratio) were blended uniformly in an autoclave, heated to 155 °C at a rate of 5 °C min^{-1}, and then held at 155 °C for 12 hours to yield the Super P /S composite. The Super P /S, Super P, and binder (PVDF) (in a 7:2:1 mass ratio) were accurately weighed, put into the mortar, and grounded for 20 min. Afterward, the mixture was further grounded with a certain amount of N-methyl-2-pyrrolidone (NMP) to obtain the slurry. The slurry was uniformly coated onto aluminum foil and subjected to vacuum drying at 60 °C for 12 hours. Subsequently, it was cut by the module with a diameter of 12 mm with the sulfur loading of 1.2 ~ 1.4 mg.

The $ZnSe-SnSe_2@OCN$ functionalized separator was prepared by a simple surface coating method, 95 wt% of $ZnSe-SnSe_2@OCN$ composites, and 5 wt% of PVDF were mixed together in NMP solvent under vigorous stirring to form a homogeneous slurry, which was then coated on pristine Celgard 2400 (PP) separator. Then, the functionalized separator was dried in oven at 60 °C for about 12 h. Finally, the obtained separator was punched into circular disks of 19 mm. The mass density was controlled to be 0.5 mg cm^{-2}. In addition, the OCN functionalized separator were also prepared in the same way as the control sample.

1.2.3 Assembly of Li-S and Li|Li symmetric batteries

The CR2032 battery is assembled with a lithium anode (15.60 mm), functionalized

Celgard 2400 (PP) separator, and commercial electrolyte (1 M LiTFSI/DOL/DME + 2 wt% LiNO$_3$). The dosage of electrolyte for each cell was maintained at 50 µL. The assembly of the Li‖Li symmetric cells is similar to the assembly of the lithium-sulfur battery described above, only the positive electrode is replaced with a lithium sheet.

1.3 Structural and Characterization

Scanning electron microscopy (SEM, S4800 Hitachi) was used to analyze the morphology. The morphology and elemental mappings were examined using the transmission electron microscope (TEM, JEM-F200). X-ray diffraction (XRD) patterns were obtained on a Smart-Lab 9kW (Rigaku, Cu Kα, λ = 1.5406 Å). The porous structure was quantified using a nitrogen adsorption apparatus (Quadrasorb SI). In nitrogen atmospheres, thermogravimetric analysis (TGA) was carried out from R.T. to 600 °C (NETZSCH STA449) with temperature steps of 10 °C min^{-1}. The UV-Vis spectrum was obtained using a spectrophotometer (UV2310II). The chemical composition and bonding were investigated utilizing X-ray photoelectron spectroscopy with an excitation source of Al K X-ray (XPS, Kratos AXIS SUPRA+).

1.4 Electrochemical Measurement

The GCD, C-rate, and long-term cycling at a voltage of 1.6 to 2.8 V (vs Li$^+$/Li) was conducted on the electrochemical equipment (Land CT2001). The electrochemical characterization of Li‖Li symmetric cells was also carried out using an electrochemical workstation (Land CT2001). The areal capacity was fixed at 0.5 mAh cm^{-2}, with a cycling current density of 0.5 mA cm^{-2}. For rate performance evaluation, a current density range from 0.5 to 4 mA cm^{-2} was applied. The CV measurements were conducted on a Bio-Logic SAS (VMP-3) electrochemical workstation, with the scan rate of 0.1-0.5 mV s^{-1}, and the voltage range from 1.6 to 2.8 V (vs Li$^+$/Li). Additionally, EIS was performed over a frequency range of 100 mHz to 100 kHz. The specific capacity was calculated based on the weight of sulfur (1C = 1675 mA g-1). All electrochemical tests were performed under controlled temperature of 28 °C.

1.5 Visualizing the LiPSs Shuttling

The Li$_2$S$_6$ solution (2.5 mmol) was selected as a model for LiPS adsorption. Sublimed sulfur and Li$_2$S (5:1, n/n) were dissolved in DOL and DME (1:1, v/v) under

magnetic stirring for 48 h to yield a brown Li_2S_6 solution. For the polysulfides shuttling, the above Li_2S_6 solution was added to one side of the H-type module, and an equal amount of DOL and DME (1:1, v/v) solution was added to the other side. The setup was then allowed to stand for 6 hours.

1.6 Computational methods

The density functional theory (DFT) calculations were performed using DS-PAW software[3] and Vienna ab initio Simulation Package (VASP)[4]. Device Studio program provides a number of functions for performing visualization, modeling and simulation[5]. The projected augmented wave (PAW) method and PBE exchange-correlation functional are utilized to describe the electron-ion interaction[6] and exchange-correlation energy[7]. The smearing method was chosen as Gaussian and the width of smearing is 0.05 eV. The energy cutoff for a plane-wave basis set is 500 eV. There is a vacuum layer of 20 Å in the Z direction. The Brillouin zone was sampled using the Monkhrost -Pack scheme with a k-point mesh of $5 \times 5 \times 1$ in the OCN (001) system, $4 \times 4 \times 1$ in the ZnSe(111) system, and $5 \times 5 \times 1$ in the $SnSe_2$(001) system. Moreover, The ZnSe-SnSe$_2$ heterojunction structure was formed by constructing the (111) surface of ZnSe and the (001) surface of SnSe$_2$. A heterojunction interface of ZnSe-SnSe$_2$ (010) was constructed. The Brillouin zone of the supercell was sampled by a $2 \times 2 \times 1$ uniform k point mesh. When the forces on each atom were smaller than 0.02 eV Å^{-1}, the ionic was considered convergent. The adsorption energy (E_a) of the polysulfides on OCN, ZnSe-SnSe$_2$, SnSe$_2$ or ZnSe substrates was calculated as following: $Ea = E(system) - [E(sub) + E(Li_2S_n)]$, where $E(sub)$ is the energy of the clean substrate, $E(Li_2S_n)$ is the energy of the isolated polysulfides, and $E(system)$ is the energy of the polysulfides adsorbed on the substrate[8, 9].

2. Results and discussion

2.1 The results of composition and morphology analysis of OCN and precursor material ZnSn(OH)$_6$@OCN

The composition and morphology of the synthesized OCN were analyzed. Fig.

S1a shows the XRD pattern of OCN, with apparent graphite phase layer stacking occurring only in the range of 20-30°. Through SEM observation (Fig. S1b-d), the OCN has a two-dimensional layered structure, with an uneven surface featuring many folds and folded edges, which aids in the contact between the material and the electrolyte, promoting ion transport and electron transfer. The elemental mapping analysis (Fig. S1e-f) shows that the O, C, and N elements are uniformly distributed, which proves that the synthesized OCN material is a carbon material with two-dimensional lamellae and with uniform elemental distribution.

The composition and morphology of the synthesized precursor $ZnSn(OH)_6@OCN$ were analyzed. XRD test results from Fig. S2. The results showed that the synthesized precursor material exhibits diffraction peaks that perfectly match the positions of $ZnSn(OH)_6$ standard crystal PDF#73-2384, located at 22.8°, 32.4°, 52.4°, and 57.9°, corresponding to the (200), (220), (420), and (422) crystal planes of $ZnSn(OH)_6$. Additionally, weak carbon diffraction peaks can be observed in the range of 20-30°, indicating the successful composite formation of $ZnSn(OH)_6$ and carbon material. SEM analysis (Fig. 2a, Fig. S2b and 2c) reveals the uniform distribution of $ZnSn(OH)_6$ cubes with a consistent size of 100 nm on the surface and in the pores of the two-dimensional carbon substrate, confirming the successful loading of $ZnSn(OH)_6$ cubes onto the OCN substrate and the preparation of the precursor $ZnSn(OH)_6@OCN$.

2.2 Calculation process of the ZnSe-SnSe$_2$ content in ZnSe-SnSe$_2$@OCN from TGA

The content of ZnSe-SnSe$_2$ in ZnSe-SnSe$_2$@OCN was measured by TGA (Fig. 2c), and analyzed based on the weight loss of carbon combustion and the oxidation from ZnSe-SnSe$_2$ to ZnO-SnO$_2$ (Fig. 4i) ($OCN + O_2 \rightarrow N_2\uparrow + CO_2\uparrow$, $SnSe_2 + 3O_2 \rightarrow SnO_2 + SeO_2\uparrow$, $2ZnSe + 3O_2 \rightarrow 2ZnO + 2SeO_2\uparrow$)

$$ZnSe\text{-}SnSe_2(wt\%) = \frac{\text{Initial weight of ZnSe - SnSe2}}{\text{Initial weight of ZnSe - SnSe2@OCN}}$$

$$= \frac{\text{Initial weight of ZnSe - SnSe2}}{\text{Final weight of ZnO - SnO2}} \times \frac{\text{Final weight of ZnO - SnO2}}{\text{Initial weight of ZnSe - SnSe2@OCN}}$$

$$\frac{m_{SnSe2} + m_{ZnSe}}{= m_{SnO2} + m_{ZnO}} \times \frac{\text{Final weight of ZnO - SnO2}}{\text{Initial weight of ZnSe - SnSe2@OCN}}$$

$$= \frac{n \times (M_{SnSe2} + M_{ZnSe})}{n \times (M_{SnO2} + M_{ZnO})} \times \frac{\text{Final weight of ZnO - SnO2}}{\text{Initial weight of ZnSe - SnSe2@OCN}}$$

$$= \frac{M_{SnSe2} + M_{ZnSe}}{M_{SnO2} + M_{ZnO}} \times \frac{\text{Final weight of } SnO_2/ZnO}{\text{Initial weight of ZnSe - SnSe2@OCN}} = 1.81 \times W^{SnO_2}{}_{/ZnO}$$

(%)

Where M_{ZnSe}, M_{SnSe2}, M_{SnO_2} and M_{ZnO} are the molecular weight of ZnSe, SnSe$_2$, ZnO and SnO$_2$, respectively. $W^{SnO_2}{}_{/ZnO}$ is the mass ratio of ZnO-SnO$_2$. The total content of ZnSe-SnSe$_2$ in ZnSe-SnSe$_2$@OCN is calculated to be 63.3%, and the content of carbon is calculated to be 36.7%.
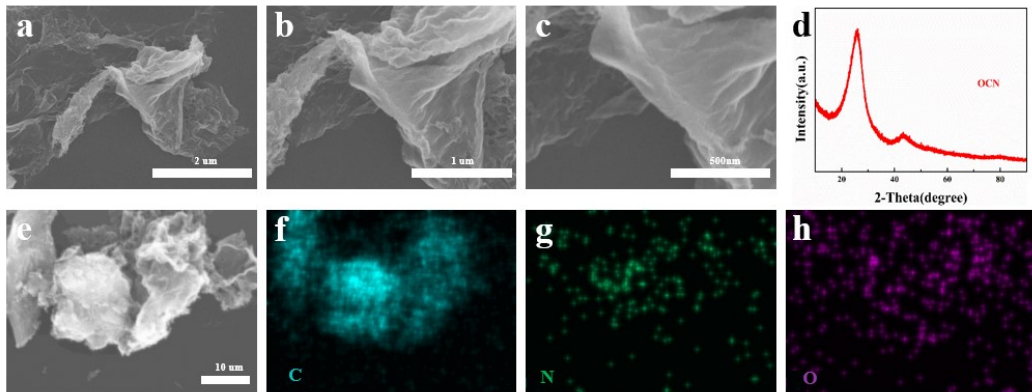
Fig. S1 Morphology and composition of the OCN. (a-c) SEM image. (d) XRD patterns. (e-h) elemental mapping of oxygen (O), carbon (C) and nitrogen (N).
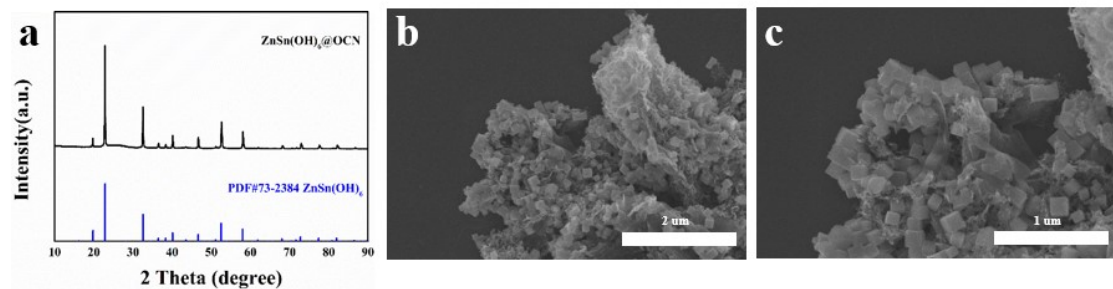
Fig. S2 The crystalline phase and morphology of the ZnSn(OH)$_6$@OCN cubes. (a) XRD patterns. (b) and (c) SEM images.
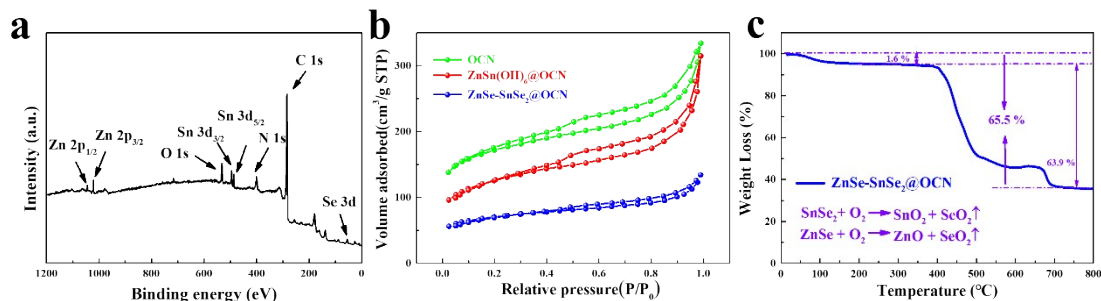

Fig. S 3 (a) XPS survey. (b) N$_2$ adsorption/desorption isotherm. (c) Thermogravimetric analysis (TGA) curve.

To investigate the specific surface area, nitrogen adsorption-desorption isotherms were conducted. Fig. S3b shows that the specific surface areas of ZnSe-SnSe$_2$@OCN, ZnSn(OH)$_6$@OCN, and OCN materials were 228.4 m^2 g^{-1}, 414.8 m^2 g^{-1}, and 629.6 m^2 g^{-1}, respectively. The OCN material exhibited a Type IV isotherm with a hysteresis loop in the moderate relative pressure range, indicating the maximization of the specific surface area due to the presence of mesopores and narrow pores. After loading ZnSn(OH)$_6$ cubes, the specific surface area sharply decreased, indicating that the formed cubes filled into the channels of OCN, consistent with the SEM image results. Finally, the ZnSe-SnSe$_2$@OCN was obtained through in-situ selenization, which had the lowest specific surface area and almost no hysteresis loop, primarily due to the agglomeration of cubes during the high-temperature selenization process. The content of SnSe/ZnSe in ZnSe-SnSe$_2$@OCN was determined by thermogravimetric analysis based on the oxidation products of SnO$_2$ and ZnO, approximately 63.3% (Fig. S3c).
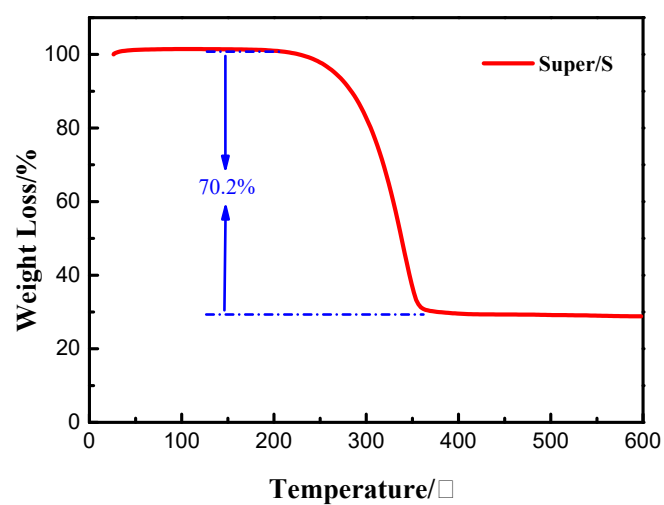
Fig. S4 Thermogravimetric analysis of Super P/S nanocomposites under N_2 atmosphere with a heating rate of 10 °C min^{-1}.
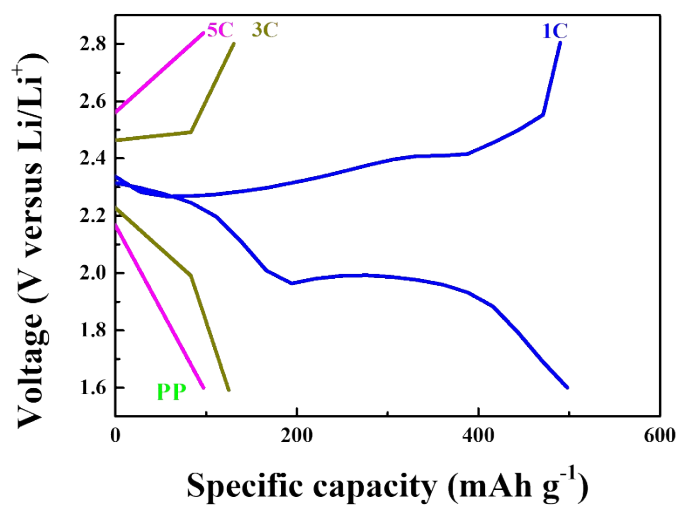

Fig. S5 The charge/discharge profiles at current densities of 1C, 3C and 5C for Li-S batteries with PP separator.
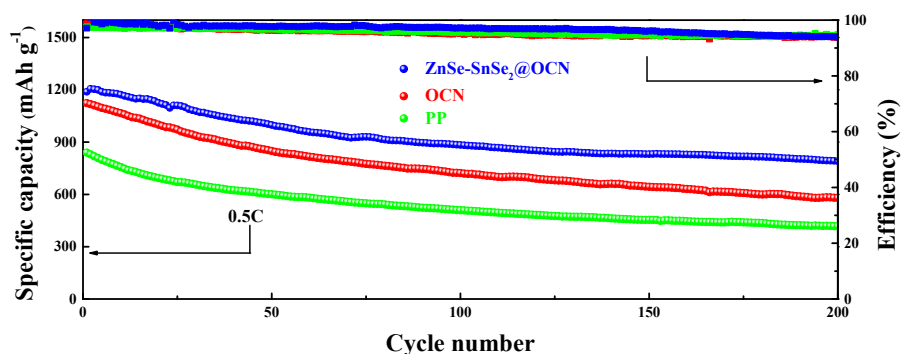
Fig. S6 Cycling performance at 0.5 C of Li-S batteries with the functionalized separators of ZnSe-SnSe$_2$@OCN, OCN and the PP control.

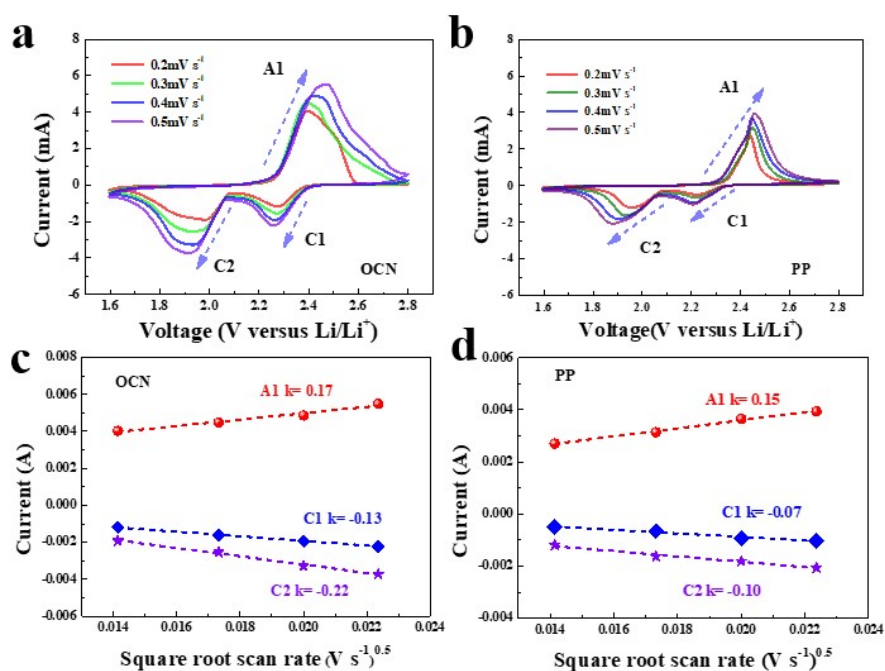**Fig. S7** Electrochemical performances of Li-S batteries with functionalized separators. The CV measured at scan rates from 0.2 to 0.5 mV s^{-1} of (a) OCN and (b) PP. The plot of Li$^+$ ion diffusion kinetics of (c) OCN and (d) PP.
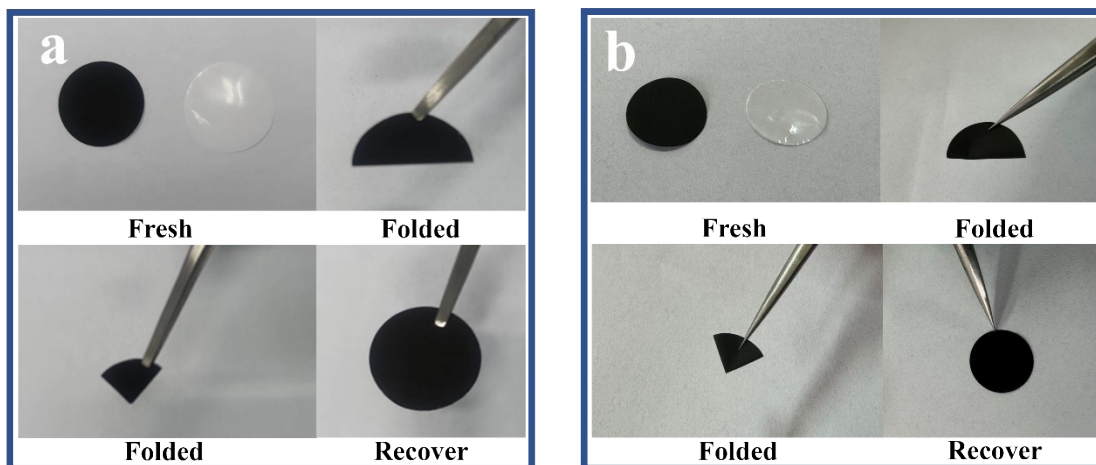
Fig. S8 Mechanical stability of functionalized separators. (a) ZnSe-SnSe$_2$@OCN and (b) OCN.
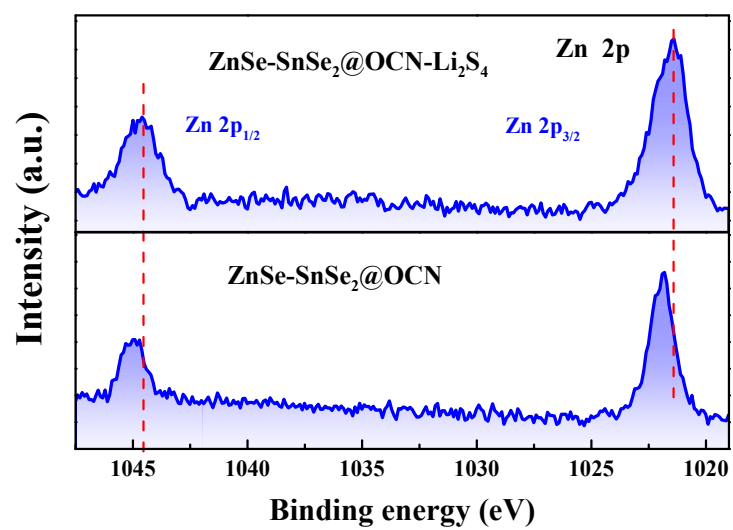

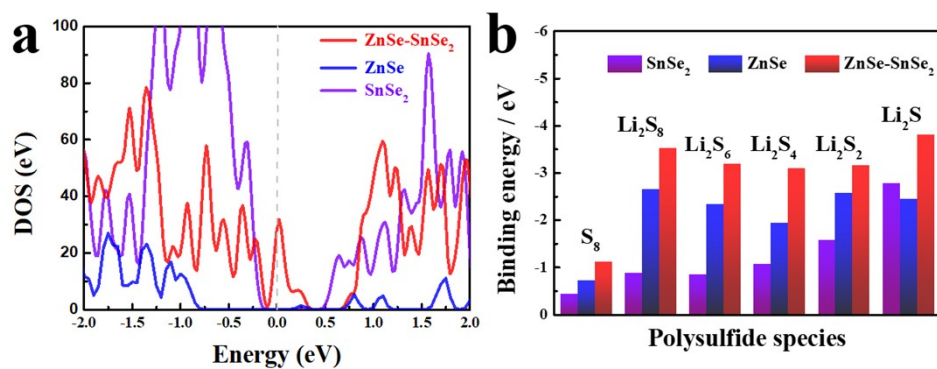**Fig. S9** High-resolution Zn 2p XPS spectra of ZnS-SnSe$_2$@OCN before and after 200 cycles.

Fig. S10 Electronic structure and binding energy of the ZnSe-SnSe$_2$. (a) Density of states (DOS) of ZnSe, SnSe$_2$ and ZnSe–SnSe$_2$. (b) Binding energies of S (S$_8$, Li$_2$S$_8$, Li$_2$S$_6$, Li$_2$S$_4$, Li$_2$S$_2$, Li$_2$S) adsorbed on ZnSe, SnSe$_2$ and ZnSe-SnSe$_2$.
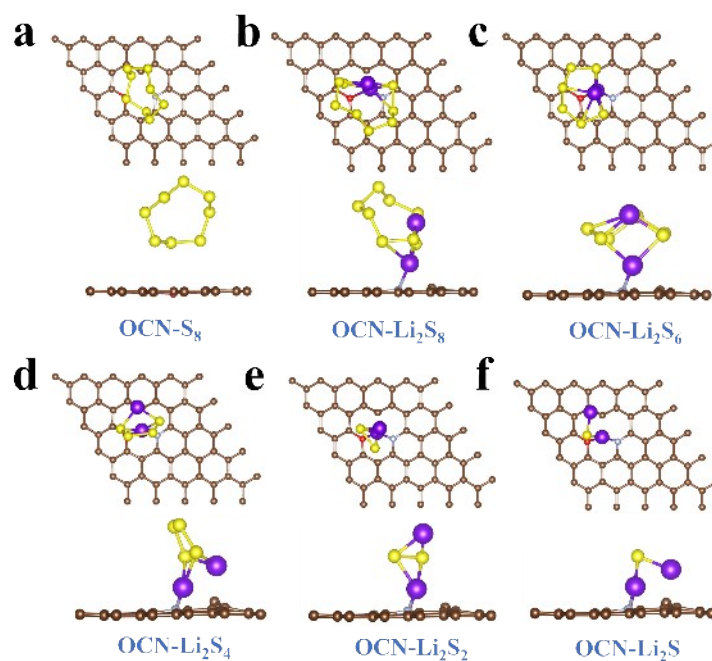
Fig. S11 Structural configurations of S species (S$_8$, Li$_2$S$_8$, Li$_2$S$_6$, Li$_2$S$_4$, Li$_2$S$_2$, Li$_2$S) adsorbed on OCN.
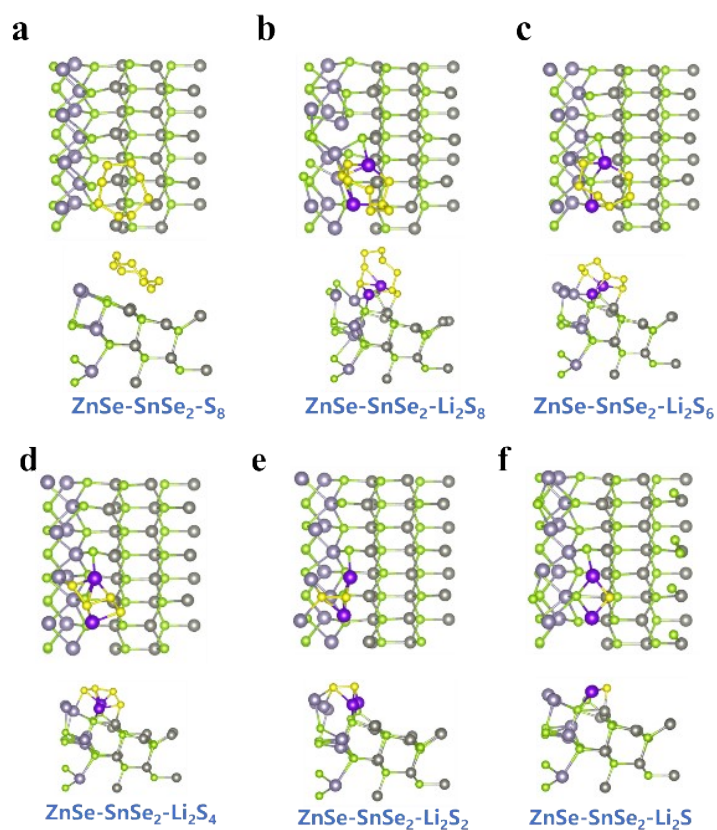
Fig. S12 Structural configurations of S species (S_8, Li_2S_8, Li_2S_6, Li_2S_4, Li_2S_2, Li_2S) adsorbed on ZnSe-SnSe$_2$.
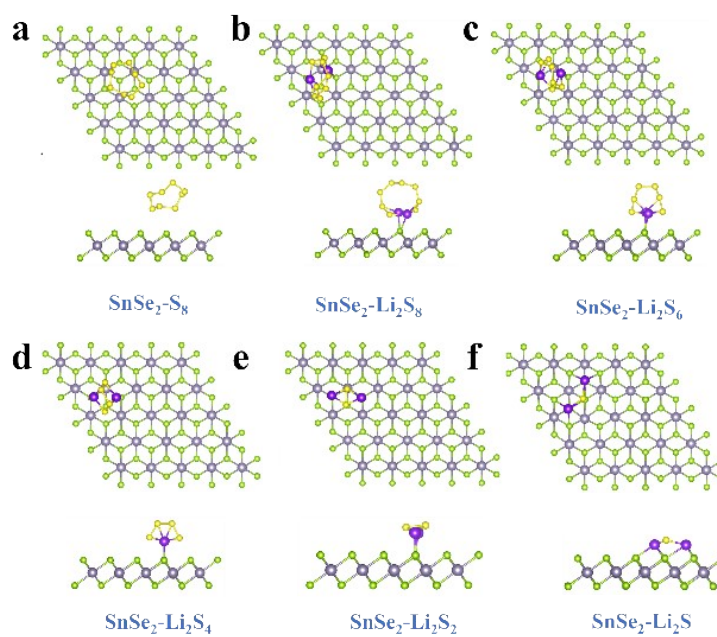
Fig. S13 Structural configurations of S species (S_8, Li_2S_8, Li_2S_6, Li_2S_4, Li_2S_2, Li_2S) adsorbed on SnSe$_2$.
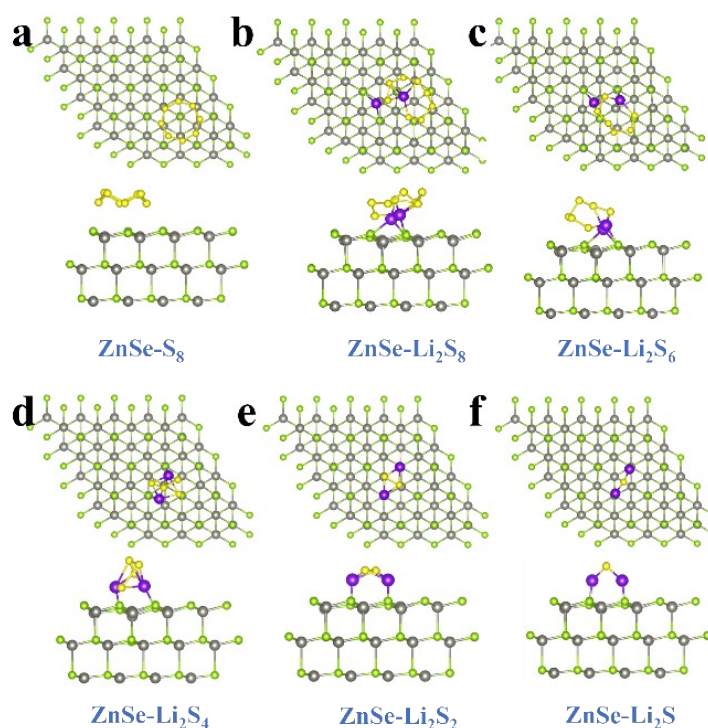
Fig. S14 Structural configurations of S species (S$_8$, Li$_2$S$_8$, Li$_2$S$_6$, Li$_2$S$_4$, Li$_2$S$_2$, Li$_2$S) adsorbed on ZnSe.

Table S1. Comparison of electrochemical performance of Li-S batteries with functionalized separator

Functionalized separator	Carrying capacity	Initial capacity	Cycling stablity	Coulomb efficiency	Ref.
MoO$_2$-CNT	2.4 mg cm^{-2}	997 mAh g^{-1}	678.2 mAh g^{-1} after 300 cycles at 0.1C	97.92%	10
CoMoO$_4$-12/PP	1.1-1.3 mg cm^{-2}	1018.5 mAh g^{-1}	745.5 mAh g^{-1} after 200 cycles at 0.2C	99.84%	11
TiO$_2$/PC	0.5mg cm^{-2}	1060 mAh g^{-1}	708 mAh g^{-1} after 150 cycles at 0.1C	99.8%	12
CFP@CN-PP	-	840 mAh g^{-1}	528.3 mAh g^{-1} after 650 cycles at 1C	99.87%	13
CuS/graphene	0.5 mg cm^{-2}	1302 mAh g^{-1}	760 mAh g^{-1} after 100 cycles at 0.2C	-	14
Co-N-C@PE	0.3 mg cm^{-2}	824 mAh g^{-1}	725mAh g^{-1} after 200 cycles at 0.5C	99.93%	15
KB-MnO	1.5-2mg cm^{-2}	1059 mAh g^{-1}	901mAh g^{-1} after 200 cycles at 1C	99.91%	16
CNFs/CoS$_{2-x}$	0.778mg cm^{-2}	907.5 mAh g^{-1}	528 mAh g^{-1} after 370 cycles at 1C	95.6%	17
FeS$_2$@MMT/PP	0.25 mg cm^{-2}	1016 mAh g^{-1}	736 mAh g^{-1} after 800 cycles at 1C	99.96%	18
ZnSe-SnSe$_2$@OCN	0.5 mg cm^{-2}	1265 mAh g^{-1}	661 mAh g^{-1} after 350 cycles at 1C	98.6%	This work

Table S2. The binding energies for S species adsorbed on OCN and ZnSe-SnSe$_2$.

	S$_8$	Li$_2$S$_8$	Li$_2$S$_6$	Li$_2$S$_4$	Li$_2$S$_2$	Li$_2$S
OCN	-0.43	-1.14	-1.28	-1.23	-1.48	-1.62

ZnSe-SnSe$_2$	-1.12	-3.53	-3.18	-3.09	-3.17	-3.81

Table S3. The binding energies for S species adsorbed on SnSe$_2$ and ZnSe.

	S$_8$	Li$_2$S$_8$	Li$_2$S$_6$	Li$_2$S$_4$	Li$_2$S$_2$	Li$_2$S
SnSe$_2$	-0.44	-0.88	-0.85	-1.07	-1.57	-2.78
ZnSe	-0.71	-2.65	-2.34	-1.94	-2.58	-2.44

References

1. J. Liu, S. Xie, Z. Geng, K. Huang, L. Fan, W. Zhou, L. Qiu, D. Gao, L. Ji, L. Duan, L. Lu, W. Li, S. Bai, Z. Liu, W. Chen, S. Feng and Y. Zhang, Carbon nitride supramolecular hybrid material enabled high-efficiency photocatalytic water treatments, *Nano Letters*, 2016, **16**, 6568-6575.

2. J. Liu, W. Li, L. Duan, X. Li, L. Ji, Z. Geng, K. Huang, L. Lu, L. Zhou, Z. Liu, W. Chen, L. Liu, S. Feng and Y. Zhang, A graphene-like oxygenated carbon nitride material for improved cycle-life lithium/sulfur batteries, *Nano Letters*, 2015, **15**, 5137-5142.

3．P. E. Blöchl, Projector augmented-wave method, *Physical Review B*, 1994, **50**, 17953–17979.

4. G. Kresse and J. Furthmuller, Efficient iterative schemes for ab initio total-energy calculations using a plane-wave basis set, *Physical Review B*, 1996, **54**, 11169-11186.

5. Device Studio, Version 2022B, Hongzhiwei Technology, China, 2021. Available online:https://iresearch.net.cn/cloudSoftware accessed on September, 11.

6. G. J. 1 Kresse, D., From ultrasoft pseudopotentials to the projector augmented-wave method. , *Physical Review B*, 1999, 1758-1774.

7. K. B. J. P. Perdew, and M. Ernzerhof, Generalized gradient approximation made

simple, *Physical Review Letters*, 1996, 3865-3868.

8.   W. Yao, W. Zheng, J. Xu, C. Tian, K. Han, W. Sun and S. Xiao, ZnS-SnS@NC heterostructure as robust lithiophilicity and sulfiphilicity mediator toward high-rate and long-life lithium-sulfur batteries, *ACS Nano*, 2021, **15**, 7114-7130.

9.   Z. Yang, C. Peng, R. Meng, L. Zu, Y. Feng, B. Chen, Y. Mi, C. Zhang and J. Yang, Hybrid anatase/rutile nanodots-embedded covalent organic frameworks with complementary polysulfide adsorption for high-performance lithium-sulfur batteries, *ACS Central Science*, 2019, **5**, 1876-1883.

10.   C. Choi, D.-Y. Lee, J. B. Park, D.-W. Kim, Separators Modified Using MoO_2@Carbon Nanotube Nanocomposites as Dual-Mode Li Polysulfide Anchoring Materials for High-Performance Anti-Self-Discharge Lithium-Sulfur Batteries, *ACS Sustainable Chemistry & Engineering*, 2020, **8**, 15134-15148.

11.   M. Huang, X. Jiang, C. Xu, S. Zhao, S. Zhang, G. Li, $CoMoO_4$ Nanorods Coated Separator for High-Performance Lithium Sulfur Batteries. *Materials Chemistry and Physics*, 2023, **295**, 127182.

12.   H. Han, S. Niu, Y. Zhao, T. Tan, Y. Zhang, TiO_2/Porous Carbon Composite-Decorated Separators for Lithium/Sulfur Battery. *Nanoscale Research Letters*, 2019, **14**:176.

13.   T. Yoo, J. Y. Maeng, S. Park, M. Bae, Y. Kim, J. Choi, H. Hong, S. J. Hwang, E. Lee, Y. Piao, Co-Fe Phosphide@Graphitic Carbon Nitride Nanosheet Modified Separator for High-Performance Lithium-Sulfur Batteries. *Journal of Alloys and Compou*nds 2023, **949**, 169873.

14.   H. Li, L. Sun, Y. Zhao, T. Tan, Y. Zhang, A Novel CuS/Graphene-Coated Separator for Suppressing the Shuttle Effect of Lithium/Sulfur Batteries. *Applied Surface Science*, 2019, **466**, 309-319.

15.   L. Jin, Z. Fu, X. Qian, B. Huang, F. Li, Y. Wang, X. Shen, Catalytic Co-N-C Hollow Nanocages as Separator Coating Layer for Lithium-Sulfur Batterys. *Microporous and Mesoporous Materials*, 2021, **316**, 110927.

16.   X. Qian, L. Jin, D. Zhao, X. Yang, S. Wang, X. Shen, D. Rao, S. Yao, Y. Zhou,

X. Xi,Ketjen Black-MnO Composite Coated Separator for High Performance Rechargeable Lithium-Sulfur Battery. *Electrochimica Acta*, 2016, **192**, 346-356.

17. X. Men, T. Deng, X. Li, L. Huang, J. Wang, Electrospun Carbon Nanofibers Loaded with Sulfur Vacancy CoS_2 as Separator Coating to Accelerate Sulfur Conversion in Lithium-Sulfur Batteries. *Journal of Colloid and Interface Science*, 2025, **678**, 345-354.

18. L. Wu, Y. Zhao, Y. Yu, B. Liao, H. Pang, H. Xie, FeS_2 intercalated Montmorillonite as a Multifunctional Separator Coating for High-Performance Lithium-Sulfur Batteries. *Inorganic Chemistry Frontiers*, 2023, **10**, 651-665.